Chapter 7
Wave Control in Hierarchical Kerf Structures

Samuel Crawford, Kanak Mantri, Mihir Patil, Marcia A. Cooper*, **and Anastasia Muliana**

Abstract The purpose of this research is to understand the energy storing, dissipation abilities, and stress wave propagation in three-dimensional kerf structures under dynamic impact loading conditions. We study a square kerf pattern made of multiple polymer materials. The first approach uses a single polymer of either brittle polylactic acid (PLA) or compliant thermoplastic polyurethane (TPU). The second approach uses a programmable filament (PF) having a mixture of PLA and TPU to create composite microstructures with alternating brittle and compliant materials. The deformation responses indicated that the cell reconfigurations, from buckling and densification, and cell fracture during loading contribute to energy dissipation while energy storing is attributed to the material elastic responses. We expect that by tuning kerf geometrical parameters and altering materials within the kerf structures, we can control wave propagation and energy management. To understand the dynamic response and deformation patterns, the kerf structures are subjected to intermediate impact from a split Hopkinson pressure bar (SHPB) facility. During testing, kerf structure deformation is recorded at high speed and strain gauge signals are recorded. The experimental deformation patterns and stress wave propagation responses are simulated using ABAQUS FEA. We first establish material models for the 3D printed materials at high strain rates, demonstrating the ability to simulate their material responses in dynamic compression, and then explore the energy dissipation and stress wave propagation in 3D hierarchical kerf structures. Kerf structures are potentially used for controlling energy transfer under dynamics loadings.

Keywords Kerf Structure · Dynamic Impact · Wave Propagation

Introduction

Recent advancements in manufacturing techniques and technologies allow for the creation of complex geometrical structures that exhibit improved mechanical properties beyond the base material. In this study, we adopt a kerfing topology, traditionally used in wood cutting, to create thick and flexible structures that are reconfigurable to complex geometries [1]. Studies in planar and thin-walled kerf structures show that the structures can be used to control wave propagation and energy dissipation through the structure [2, 3]. These properties of kerf structures make them potentially beneficial in engineering applications where energy management is required in a dynamic, high-stress environment, such as in aerospace or defense [4, 5]. By utilizing 3D printing technology, it is possible to create kerf structures additively using a range of polymers with widely varying material properties. Some studies have already explored the energy absorption capabilities of 3D printed lattice and cell structures at low strain rates [6–8].

In high strain rate environments, kerf structures may exhibit unique energy dissipation capabilities which are largely unstudied. The split-Hopkinson pressure bar apparatus is a standard method for material characterization at high strain rates [9, 10]. In this study, we characterize the stress-strain behavior of a 3D printed kerf structure made of several different polymer materials, including PLA, TPU, and PF based on combinations of 0.5 PLA and 0.5 TPU by volume [11].

Samuel Crawford · Kanak Mantri · Mihir Patil · Marcia A. Cooper · Anastasia Muliana
J. Mike Walker '66 Department of Mechanical Engineering
e-mail: spcrawford@tamu.edu; kanakmantri@tamu.edu; mihirpatil@tamu.edu; macoope@tamu.edu; amuliana@tamu.edu

Marcia A. Cooper
Materials Science and Engineering Department
Texas A&M University, College Station, Texas, USA 77843
e-mail: macoope@tamu.edu

Paul Allison et al. (eds.), *Dynamic Behavior of Materials, Vol. 1*, Conference Proceedings
of the Society for Experimental Mechanics Series, https://doi.org/10.13052/97887-438-0827-5_7

Materials and Methods

Two different structures were tested – short disks to establish material stress-strain behavior, and kerf structures to investigate energy management behaviors (Fig. 1). Each structure was 3D printed in PLA, TPU, or the custom blended PF. All samples were printed using a Bambu Lab P1P 3D printer with a 0.4 mm nozzle with a bed temperature of 60 ℃, a layer height of 0.2 mm, and 100% in-fill. The PLA samples were printed using Overture 3D 1.75 mm diameter PLA filament with a printing temperature of 210 ℃. TPU samples were printed using Overture 3D 1.75 mm diameter TPU filament with a printing temperature of 220 ℃. PF samples were printed at 235 ℃ with a filament having a parallel arrangement of PLA and TPU with 50:50 volume ratio.

Fig. 1 Photographs of 3D printed disk and square kerf structure

The samples were tested in high strain rates with a conventional split Hopkinson pressure bar apparatus (SHPB, Fig. 2) consisting of a gas gun, striker bar, incident bar, transmission bar, and data measurement and acquisition system. In this standard test setup, the three bars are the same material and diameter. The sample is positioned in between and in contact with the incident and transmission bar. The gas gun launches the striker bar to impact the free end of the incident bar. The compressive pulse generated from this impact then travels through the incident bar until reaching the sample, where the impedance mismatch reflects a tensile pulse back through the incident bar and transmits a compression pulse through to the transmission bar. Our SHPB was fabricated by Dynamic Systems and Research, Inc. and utilizes a 25.4-mm diameter aluminum 7075-T6 compression bar set (incident bar length of 3.05 m and transmission bar length of 2.44 m). Striker bar velocity is measured with a Dynamic Systems & Research model DSR-1031 laser sensor.

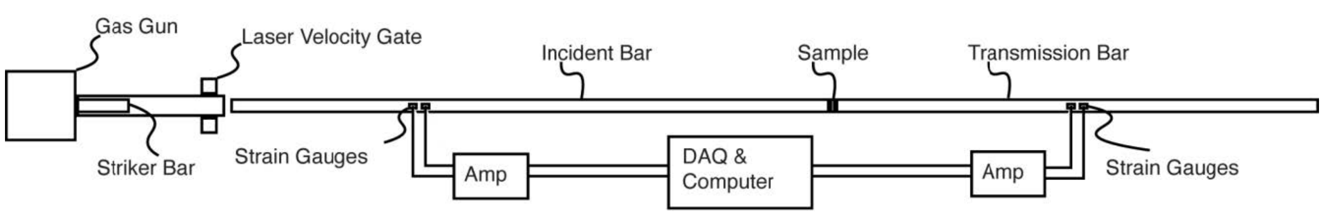

Fig. 2 Diagram of the split-Hopkinson pressure bar apparatus

Strain gauges on the incident and transmission bar measure the incident pulse strain (ε_i), reflected pulse strain (ε_r), and transmitted pulse strain (ε_t) histories. Two separate strain gauges each are attached to the incident and transmission bars – one Micro-Measurements EA-06-125BZA-350/E 350-Ohm strain gauge, and one Micro-Measurements WK-13-125BZ-10C 1000-Ohm strain gauge. Each strain gauge is connected to a Vishay Measurements Group Model 2310B signal conditioning amplifier. Signals from all the amplifiers and the velocity sensor are collected by a National Instruments cDAQ chassis and modules at a sampling rate of 2 MHz.

These measured strains allow for the calculation of sample stress (σ), strain rate ($\dot{\varepsilon}$), and strain (ε) by the following equations [9, 10]:

$$\sigma\left(t\right) = \frac{AE}{2A_s}\left(\varepsilon_i + \varepsilon_r + \varepsilon_t\right) \# \left(1\right)$$

$$\dot{\varepsilon}(t) = \frac{2c_b\varepsilon_r}{A_s} \# \left(2\right)$$

$$\varepsilon(t) = \int_0^t \dot{\varepsilon} d\tau \# \left(3\right)$$

where A is the cross-sectional area of the bars, E is the Young's modulus of the bars, A_s is the instantaneous cross-sectional area of the sample, and c_b is the bar sound speed. Thus, the stress-strain behavior of the sample material at the tested strain rate is calculated. This analysis is called a 3-wave analysis, for its use of the incident, reflected, and transmitted waves to calculate the sample stress [9].

This analysis relies on the assumption of force equilibrium at the sample faces in contact with the bars which occurs within a short transient for ductile materials and long compressive pulse durations. In compliant materials, achieving force equilibrium can be challenging and requires pulse shaping — the addition of a sacrificial, plastically deforming material to introduce a slope to the incident pulse that ramps the strain slowly — allowing the front and back stresses of the sample to remain in equilibrium for the duration of the pulse. To observe the stress-strain material behavior of the short disk samples, a series of different pulse shapers was used to achieve force equilibrium in the samples. For the PLA samples, a combination of copper and aluminum pulse shapers were used together as a dual pulse shaper. The aluminum and copper were both disks 8.95 mm (0.3525 inch) in diameter. The aluminum was 0.127 mm (0.005 inch) thick and placed against the incident bar free end. The copper was 0.8255 mm (0.0325 inch) thick and placed between the striker bar and the aluminum pulse shaper. In the case of TPU, a closed-cell neoprene foam was used. The neoprene pulse shapers were cylinders with a diameter and height each 12 mm. Due to limited number of samples, the PF samples were tested with the same pulse shaper used with the PLA and TPU tests.

As shown in Fig. 1, the size of the square kerf structure (29.0 mm $\times$ 29.0 mm) is greater than the SHPB bar diameter (25.4 mm) which was addressed by adding platens at the sample end of the incident and transmission bars for additional contact area (Fig. 3). The platens were attached to the bars via a threaded connection with thread relief to allow for a flat, parallel, intimate contact between the end of the bar and the inside face of the platen. The platens were designed and manufactured to maintain the standard best practices for SHPB interfacial flatness and parallelism. The diameter of the platen expands from the 25.4-mm bar diameter to a diameter of 63.5 mm (2.50 inch) over a length of 14.0 mm (0.550 inch).

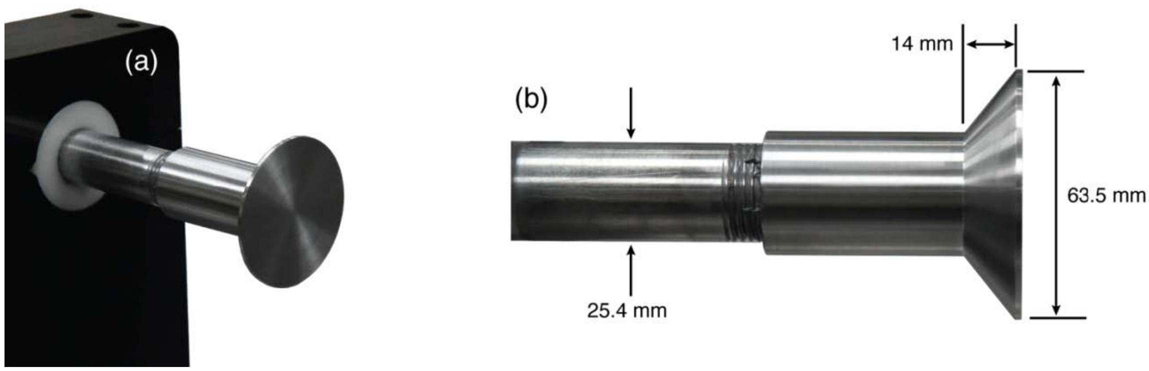

Fig. 3 Photographs of the incident bar with platen installed. An identical platen was also installed similarly on the transmission bar (not shown).

It is readily acknowledged that the area change of the platens causes the experimental method to deviate from the 1D assumptions of a traditional SHPB test. Bar-on-bar tests with the platens installed showed minor effect on the reflected and transmitted bar strains. Additionally, no pulse shaping was used when testing the kerf structures. As our motivation is to explore the effect kerf structure and material design, the platens enable large-scale structures to be explored while still enabling relative comparisons to be made. Complimentary FE simulations further extend our ability to attribute changes in energy management to material or structure effects. High speed video of the structures during dynamic compression were captured with a Photron SA-Z camera recording at 50 MHz.

Material characterization results

Experiments were performed to assess the dynamic stress-strain behavior of the three 3D-printed materials of the short disk samples. Fig. 4 (a) plots the stress-strain data for PLA under dynamic compression and modest strain rates between 170 - 490 s^{-1}. Repeat tests were performed under nominally similar impacts—striker velocity and pulse shaping—and average strain rates with standard deviations are reported with the data groupings in Fig. 4 (a). The brittle PLA transmitted most of the incident wave as observed in the strain data of Fig. 4 (b) where there is a minor difference between the incident (I) and transmitted (T) signals. At these low strain rates, evidence of damage was not visible on the external surfaces in post-test inspections. Although the PLA material under the above strain rates shows significant rate-dependent effect, it does not seem to dissipate energy.

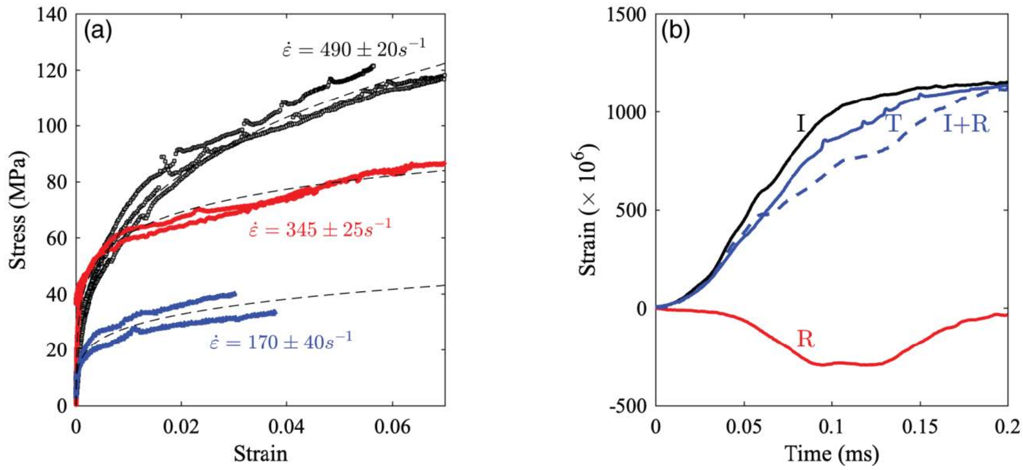

Fig. 4 (a) The strain histories of PLA under compression loading with reported average strain rate for each test. The reported strain rates are the average and standard deviation of near-replicate test conditions. (b) The strain signals reported from the I: incident, T: transmitted, R: reflected gauges for the test plotted in (a) at $\dot{\varepsilon} = 490\ \text{s}^{-1}$

Fig. 5 (a) plots the stress-strain data for TPU under dynamic compression and higher strain rates between 1370 - 2190 s^{-1}. The compliant TPU deformed at much higher strain rates without evidence of damage. This material also reflected most of the incident wave as observed in the strain data of Fig. 5 (b) where there is a minor difference between the incident (I) and reflected (R) signals. The compliant TPU deformed significantly under dynamic compression absorbing the kinetic energy and storing them as elastic energy, allowing the TPU to regain its original shape after deformation.

Fig. 6 (a) plots the stress-strain data for PF under dynamic compression and higher strain rates between 1410 - 1810 s^{-1}. A repeat test was performed and the average strain rate with standard deviation is reported. It is interesting that the PF (a 50:50 volume mixture of PLA and TPU) exhibits a low sensitivity to strain rate, whereas independently PLA (Fig. 4 (a)) and TPU (Fig. 5 (a)) both showed a clear dependence on strain rate. The PF maximum strain and stress were more like TPU versus PLA as shown in Fig. 6 (b) for two tests with similar strain rate histories. Thus, mixture ratio does not define bulk behavior of these printed composite materials—as the PF stress-strain behavior is not simply an average of the individual PLA and TPU responses—but suggests that the composite material behavior may be 1) controlled by the behavior of the most compliant component or 2) strongly influenced by the interlayer bonding and adhesion of the printing process, or 3) some combination of these effects.

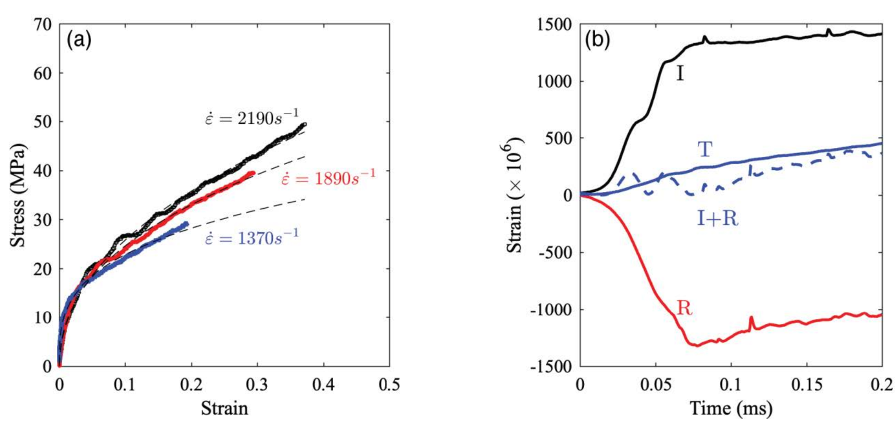

Fig. 5 (a) The strain histories of TPU under compression loading with reported average strain rate for each test. (b) The strain signals reported from the I: incident, T: transmitted, R: reflected gauges for the test plotted in (a) at $\dot{\varepsilon} = 2190\ \text{s}^{-1}$

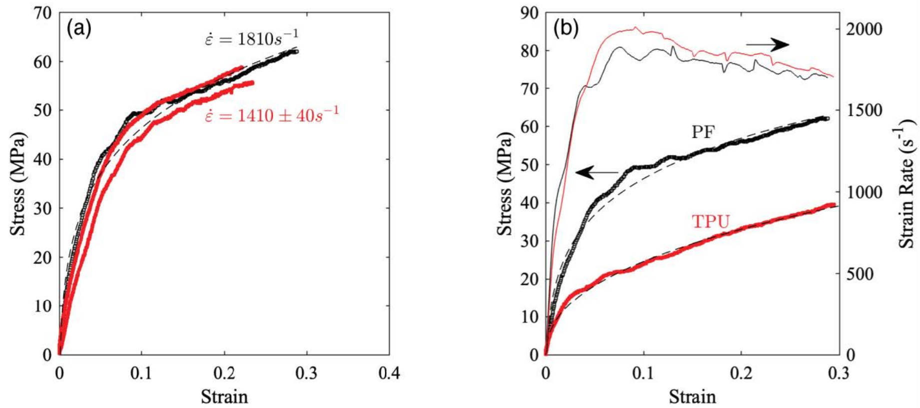

Fig. 6 (a) The strain histories for the PF under compression loading. The reported strain rates are the average and standard deviation of nominally similar test conditions. (b) A comparison of the TPU and PF stress-strain curves for the PF and TPU at similar strain rate conditions

Material model applied to square kerf structure

Using the data of Fig. 4 (a), Fig. 5 (a), Fig. 6 (a) for the three individual materials, simulations were performed on the short disk samples to demonstrate model capability. First, bar-on-bar simulations matched experimental elastic wave propagation including pulse durations and amplitudes. Then, simulated and experimental data for PLA are presented for PLA in Fig. 7 (a) for the short disk and in Fig. 7 (b) for the square kerf structure. We represented these materials with a Johnson-Cook rate-dependent material model, suitable for capturing the stress-strain responses shown above. The PLA disk transmits most of the incident stress wave, while the buckling/bending of kerf connectors alter the stress wave propagation, i.e., reducing transmission and increasing reflection. It is believed that deformations of kerf connectors enable the PLA kerf structure to partially absorb kinetic energy. Future study can optimize the geometrical parameters in PLA kerf structures to control wave propagation.

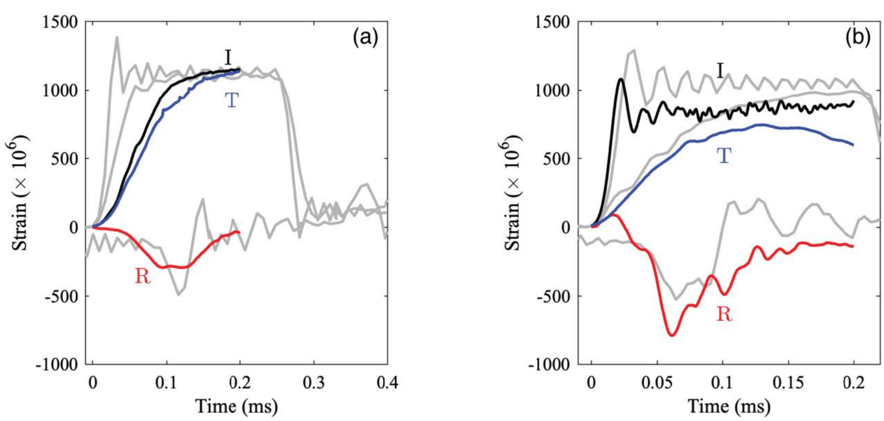

Fig. 7 Comparison of the experimental (solid-colored lines) and the simulated (gray lines) strain histories from the I: incident, T: transmitted, R: reflected gauges for (a) PLA disk sample and (b) square kerf structure. In all cases, the incident strain signal was nearly constant at 1000 μstrain. The experimental data in (a) is from Fig. 4 for $\dot{\varepsilon} = 490 \pm 20$ s^{-1}

The simulated bar strains in Fig. 7 (b) resulted in the calculated stresses within the square kerf structure shown in the top row of images in Fig. 8. The incident bar-platen is at the left—and transmitted platen-bar at the right—with the annotated arrow indicating the direction of incident wave propagation. The wave is observed to enter the kerf structure until 21 μs and then is reflected at the transmitted platen interface. After 21 μs, the kerf structure is at a nominally uniform and elevated stress level for the remaining duration of the compression pulse. The bottom row of images in Fig. 8 are successive frames of the high-speed video collected over a longer time than the simulation images. While passage of the wave is not experimentally visible (but possibly observable with future coupling of digital image correlation method), a qualitative comparison of the kerf structure deformation in the experimental (150 μs) and simulated (132 us) images show reasonable agreement. Future work will incorporate models breaking of the sample after the ultimate stress is reached which will be necessary to represent the experimental data (e.g., Fig. 8 at 250 μs).

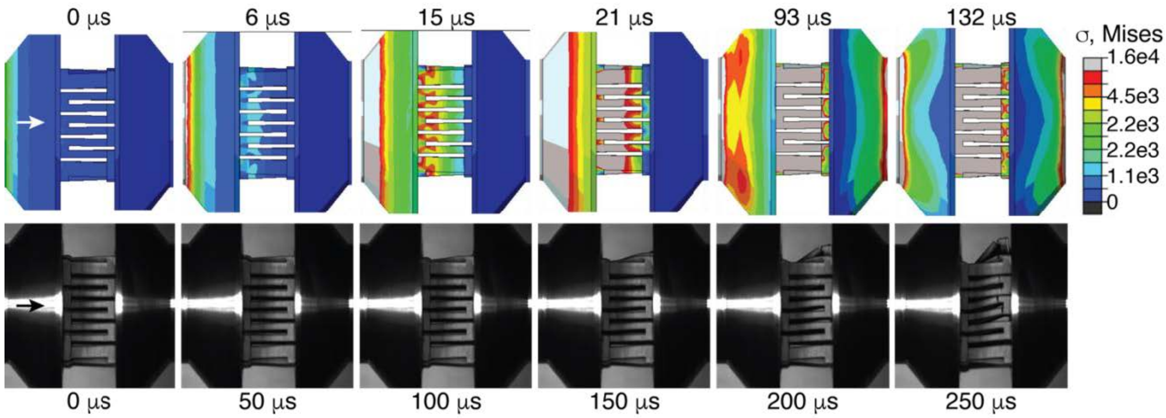

Fig. 8 Top row: simulation results for early times during arrival of the incident compression stress pulse corresponding to the simulated strain data of **Fig. 4** (b). Colorbar corresponds to Mises stresses in psi. Bottom row: a series of successive images captured at 50 MHz corresponding to the experimental strain data of **Fig. 4** (b). Incident bar with platen is at left and the transmitted bar with platen is at right

The deformation behaviors of the square kerf structures are compared in Fig. 9 for the PLA (top row of images) and PF (bottom row of images). Note that the images are provided over a longer time with zero time corresponding to the image before first motion of the incident platen is observed. The kerf structures for both materials fractured although the PF undergoes bending and densification before fracture because it is softer than PLA. PF failure appears to initiate at the long connectors. The stiff PLA does not show connector buckling prior to fracture, rather PLA failure starts at the junction of the connectors and cells. This early investigation presents opportunities to control wave propagation by tuning the materials and geometry of hierarchical kerf structures.

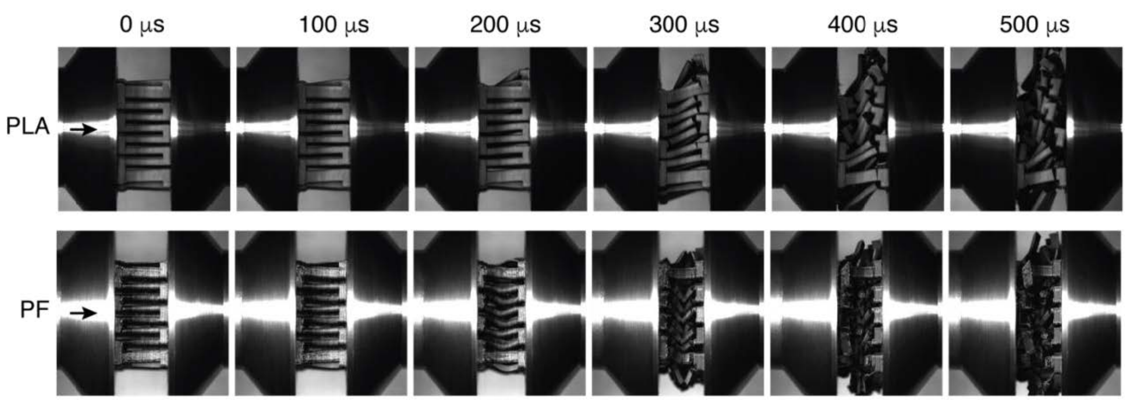

Fig. 9 Top row: a series of successive images during the dynamic compression of the PLA square kerf structure. Bottom row: a series of successive images during the dynamic compression of the PF square kerf structure. Equivalent test conditions with an incident strain of 800 μstrain. Incident bar with platen is at left and the transmitted bar with platen is at right

Conclusions

A collaborative experimental and computational study of energy management in a novel 3D kerf structure is presented. Individual materials of PLA, TPU and a 50:50 mixture by volume of a PF were studied in traditional disk samples for the collection of material stress-strain data and in novel 3D kerf structures. While the PLA exhibited brittle, low strain and high stress to failure and the TPU exhibited compliant, large deformations with recovery, the PF did not exhibit a mean behavior. Rather, the PF was interestingly insensitive to strain rate effects and exhibited behaviors like the more compliant TPU. The PF kerf structure exhibited an earlier onset of severe deformation and fracture as compared to the PLA kerf structure. This work is ongoing with additional investigations exploring the sensitivity of bulk behavior on material and kerf structure design.

Acknowledgments This work was supported by a 2023-2024 MEEN Seed Grant within the J. Mike Walker '66 Department of Mechanical Engineering at Texas A&M University.

References

1. Bianconi F, Filippucci M (2019) Digital wood design: innovative techniques of representation in architectural design. Springer
2. Shahid Z, Bond CG, Johnson MS, et al (2022) Dynamic response of flexible viscoelastic kerf structures of freeform shapes. *Int J Solids Struct* 254–255. https://doi.org/10.1016/j.ijsolstr.2022.111895
3. Shahid Z, Hubbard JE, Kalantar N, Muliana A (2022) An investigation of the dynamic response of architectural kerf structures. *Acta Mech* 233:157–181. https://doi.org/10.1007/s00707-021-03108-z
4. Murray CM, Mao M, Park J, et al (2023) Visco-Elastic Honeycomb Structures with Increased Energy Absorption and Shape Recovery Performance Using Buckling Initiators. *Polymers* (Basel) 15. https://doi.org/10.3390/polym15163350
5. Rudykh S, Ortiz C, Boyce MC (2015) Flexibility and protection by design: Imbricated hybrid microstructures of bio-inspired armor. *Soft Matter* 11:2547–2554. https://doi.org/10.1039/c4sm02907k
6. Nam R, Jakubinek M, Niknam H, et al (2023) 3D printed octet plate-lattices for tunable energy absorption. *Mater Des* 228. https://doi.org/10.1016/j.matdes.2023.111835
7. Kumar A, Verma S, Jeng JY (2020) Supportless lattice structures for energy absorption fabricated by fused deposition modeling. 3D Print *Addit Manuf* 7:85–96. https://doi.org/10.1089/3dp.2019.0089
8. Tsouknidas A, Pantazopoulos M, Katsoulis I, et al (2016) Impact absorption capacity of 3D-printed components fabricated by fused deposition modelling. *Mater Des* 102:41–44
9. Gray III GT (2002) High-Strain-Rate Testing of Materials. Characterization of Materials
10. Chen WW, Song B (2010) Split Hopkinson (Kolsky) bar: design, testing and applications. Springer Science & Business Media
11. Darnal A, Shahid Z, Deshpande H, Kim J, and Muliana A, (2023) Tuning Mechanical Properties of 3D Printed Composites with PLA:TPU Programmable Filaments. *Composite Structures*, 318,117075.